The Astrophysical Journal, 788:3 (14pp), 2014 June 10 doi:10.1088/0004-637X/788/1/3

CHARACTERIZING THE STRUCTURE OF DIFFUSE EMISSION IN Hi-GAL MAPS

D. Elia[1], F. Strafella[2], N. Schneider[3], R. Paladini[5], R. Vavrek[6], Y. Maruccia[2], S. Molinari[1], A. Noriega-Crespo[4,6], S. Pezzuto[4,5], K. L. J. Rygl[1,7], A. M. Di Giorgio[1], A. Traficante[8], E. Schisano[4], L. Calzoletti[9], M. Pestalozzi[1], S. J. Liu[1], P. Natoli[9,10,11,12], M. Huang[13], P. Martin[14], Y. Fukui[15], and T. Hayakawa[15]
[1] INAF-IAPS, Via Fosso del Cavaliere 100, I-00133 Roma, Italy; davide.elia@iaps.inaf.it
[2] Dipartimento di Matematica e Fisica E. De Giorgi, Università del Salento, CP 193, I-73100 Lecce, Italy
[3] Univ. Bordeaux, LAB, CNRS, UMR 5804, 33270, Floirac, France
[4] Space Telescope Science Institute, 3700 San Martin Drive, Baltimore, MD 21218
[5] Infrared Processing and Analysis Center, California Institute of Technology, Pasadena, CA 91125, USA
[6] Herschel Science Centre, European Space Astronomy Centre, Villafranca del Castillo, Apartado de Correos 78, E-28080 Madrid, Spain
[7] Research and Scientific Support Department, European Space Agency (ESA-ESTEC), P.O. Box 299, 2200-AG Noordwijk, The Netherlands
[8] Jodrell Bank Centre for Astrophysics, School of Physics and Astronomy, University of Manchester, Manchester M13 9PL, UK
[9] Agenzia Spaziale Italiana Science Data Center, c/o ESRIN, via Galileo Galilei, I-00044 Frascati, Italy
[10] Dipartimento di Fisica e Science della Terra, Università di Ferrara Via Saragat, 1, I-44100 Ferrara, Italy
[11] INFN, Sezione di Ferrara, via Saragat 1, I-44100 Ferrara, Italy
[12] INAF-IASF Bologna, Via P. Gobetti 101, I-40129 Bologna, Italy
[13] National Astronomical Observatories, Chinese Academy of Sciences, Beijing 100012, China
[14] Canadian Institute for Theoretical Astrophysics, University of Toronto, 60 St. George Street, Toronto, ON M5S 3H8, Canada
[15] Department of Physics, Nagoya University, Furo-cho, Chikusa-ku, Nagoya 464-8602, Japan
Received 2014 January 17; accepted 2014 April 4; published 2014 May 16

ABSTRACT

We present a study of the structure of the Galactic interstellar medium (ISM) through the Δ-variance technique, related to the power spectrum and the fractal properties of infrared/submillimeter maps. Through this method, it is possible to provide quantitative parameters, which are useful for characterizing different morphological and physical conditions, and better constraining the theoretical models. In this respect, the *Herschel* Infrared Galactic Plane Survey, carried out at five photometric bands from 70 to 500 μm, constitutes a unique database for applying statistical tools to a variety of regions across the Milky Way. In this paper, we derive a robust estimate of the power-law portion of the power spectrum of four contiguous $2^\circ \times 2^\circ$ Hi-GAL tiles located in the third Galactic quadrant ($217^\circ \lesssim \ell \lesssim 225^\circ$, $-2^\circ \lesssim b \lesssim 0^\circ$). The low level of confusion along the line of sight, testified by CO observations, makes this region an ideal case. We find very different values for the power spectrum slope from tile to tile but also from wavelength to wavelength ($2 \lesssim \beta \lesssim 3$), with similarities between fields attributable to components located at the same distance. Thanks to comparisons with models of turbulence, an explanation of the determined slopes in terms of the fractal geometry is also provided, and possible relations with the underlying physics are investigated. In particular, an anti-correlation between ISM fractal dimension and star formation efficiency is found for the two main distance components observed in these fields. A possible link between the fractal properties of the diffuse emission and the resulting clump mass function is discussed.

Key words: infrared: ISM – ISM: clouds – ISM: structure – methods: data analysis – methods: statistical – stars: formation

Online-only material: color figures

1. INTRODUCTION

One of the most intriguing tasks in the observational study of the interstellar medium (ISM) is to extract information about the three-dimensional structure of the clouds, starting from the two-dimensional maps of these objects, generally taken at different wavelengths and with different techniques and resolutions. Although a certain degree of self-similarity of the ISM maps over a given range of spatial scales can be visually perceived in many cases, there are numerous, more solid, arguments suggesting that this may be the case, starting from the work of Scalo (1990).

In this respect, the phenomenon mainly responsible for self-similar morphologies is turbulence. This is a largely recognized fact in molecular clouds, being a typical, scale-free phenomenon inducing fractality (see, e.g., Sreenivasan et al. 1989). Turbulence is indeed characterized by the lack of a specific length scale, then it can produce a fractal distribution of matter in a molecular cloud over a wide range of scales. Therefore, the determination of the starting and ending points of these ranges is generally considered a tentative way of determining an estimate of the turbulence injection and dissipation scales. An extensive and detailed review of the observational evidences of the presence of turbulence in molecular clouds and its role in shaping their structure in a fractal sense can be found in Vázquez-Semadeni (1999) and Schneider et al. (2011).

It is noteworthy that the ISM clouds belong to the same category as *stochastic fractals*, whose structures do not appear perfectly self similar, but rather *self-affine*: although a stochastie set and a part of it do not have exactly the same appearance, they have the same statistical properties and therefore it is still possible to use a fractal description for them.

There are many observational grounds supporting the fractal scenario. Observations of the low-J ^{12}CO and ^{13}CO emission lines in several star-forming molecular cloud complexes (e.g., Falgarone & Phillips 1996; Schneider et al. 1998; Wilson et al. 1999) show that the measured line intensities, shapes, and ratios cannot be produced in clouds of uniform gas temperature and density. This suggests that these interstellar objects are far from being homogeneous, instead being organized in small

clumps with a filling factor lower than unity (Elmegreen 1997b). Interestingly, such a structure is also able to further justify observed characteristics of the investigated region, such as, for example, the clump mass function (Shadmehri & Elmegreen 2011) and the stellar initial mass function (Elmegreen 2002). These remain meaningful observables, though in the last several years the understanding of the ISM has changed with the recognition of filaments as intermediate structures (e.g., Rosner & Bodo 1996; Wilson et al. 1999), which have definitely been found ubiquitous in recent *Herschel*[16] observations (e.g., Molinari et al. 2010a; Schisano et al. 2013). In any case, the cloud description, based on a hierarchical decomposition in recognizable substructures (Houlahan & Scalo 1992), is not incompatible with the fractal approach. Indeed Stutzki et al. (1998) have shown that these two points of view are consistent: an ensemble of clumps with a given mass and size spectrum can give rise to a fractal structure of the cloud.

Statistical descriptors, which can generally be related to the fractal properties of a cloud, are powerful methods for characterizing its structure. The techniques initially used to estimate the fractal dimension of the interstellar clouds were based on the isocontours of the images, as for example the *perimeter–ruler* and the *area–perimeter* relations (see, e.g., Sánchez et al. 2005, and references therein). Subsequently, statistical tools have been applied, namely descriptors based on the value and the spatial distribution of the single pixels, providing quantitative information on one or more aspects of the investigated morphology (a relevant portion of this information is summarized in Elmegreen & Scalo 2004). The direct estimate of the power spectrum (e.g., Ingalls et al. 2004; Miville-Deschênes et al. 2007; Martin et al. 2010; Gazol & Kim 2010) can be used to infer the fractal structure of the ISM, though to deal with real observational sets other algorithms have been demonstrated to be more adequate (Stutzki et al. 1998). Other statistical estimators are the structure function (Padoan et al. 2002, 2003; Kritsuk & Norman 2004; Campeggio et al. 2005; Gustafsson et al. 2006; Kowal et al. 2007; Rowles & Froebrich 2011), the Δ-variance (see below), the autocorrelation function (Campeggio et al. 2005), and the adapted correlation length (Cartwright et al. 2006), whereas further development of these monofractal descriptors is represented by the multifractal spectrum (Chappell & Scalo 2001; Vavrek et al. 2001). In particular, the Δ-variance method was introduced by Stutzki et al. (1998) and subsequently improved by Bensch et al. (2001) and Ossenkopf et al. (2008) to analyze the drift behavior of observed scalar functions such as the intensity distribution in molecular clouds, real or synthesized. It has been applied not only to maps of line emission (see also Bensch et al. 2001; Ossenkopf et al. 2001, 2008; Schneider et al. 2011; Rowles & Froebrich 2011) and dust extinction (Campeggio et al. 2004; Schneider et al. 2011), or emission (Russeil et al. 2013), but also to the recovered velocity field (Ossenkopf et al. 2006; Federrath et al. 2010), or to three-dimensional density fields of turbulence simulations (Federrath et al. 2009).

The aim of this paper is to contribute to both the enlargement of the sample of regions whose structural properties have been studied by means of fractal techniques, and the improvement of characterizing the response of statistical tools in different observing conditions. The Hi-GAL survey (*Herschel* Infrared GALactic plane survey; Molinari et al. 2010b) represents an extraordinary resource for carrying out statistical studies of the ISM. A large coverage is obtained in five different bands, allowing for a large variety of morphologies and physical conditions to be investigated at unprecedented spatial resolution. Moreover, these large *Herschel* maps offer the opportunity to probe a wide range of spatial scales, since the number of available pixels is very important for the reliability of the statistical descriptors.

Galactic plane observations suffer from confusion due to the superposition of different components along the line of sight, especially in the first and fourth Galactic quadrants. To minimize the problem of confusion, the first available observations of the third Galactic quadrant (in the range $217.^\circ0 \lesssim \ell \lesssim 224.^\circ3$) are studied as a first test case, in which we are more confident that the observed ISM emission corresponds to a morphology that is quite coherent from the spatial point of view. These observations have been presented by Elia et al. (2013) (hereafter Paper I), and are briefly summarized in Section 2.

As a paradigm of synthetic cloud images used for testing the statistical tools applied in this work, we consider the class of so-called *fractional Brownian motion* images (hereinafter fBm). They have already been used, for example, by Stutzki et al. (1998), Bensch et al. (2001), Khalil et al. (2006), Miville-Deschênes et al. (2007), and Shadmehri & Elmegreen (2011) to test their algorithms. We briefly discuss the properties of this class of images in Section 3.

In this paper, we adopt the Δ-variance algorithm to derive a robust estimate of the power spectrum slope of the maps. In Section 4, this method is briefly described, and its application to synthetic maps is discussed to characterize the response of the algorithm in case of the analyzed image's departure from ideal fBm-like behavior.

In Section 5, we present the results of our Δ-variance analysis and discuss the obtained power spectrum slopes and self-similarity ranges, searching for cross-correlations among different maps and observational wavebands. Moreover, links with turbulence and observables related to star formation (as star formation efficiency and mass functions) are investigated. Finally, the results are summarized in Section 6.

2. OBSERVATIONAL DATA SETS

The *Herschel* (Pilbratt et al. 2010) open time key project, Hi-GAL (Molinari et al. 2010b), is a five-band photometric survey which was initially aimed at studying stellar life cycles in the inner Galaxy ($-72^\circ \lesssim \ell \lesssim 68^\circ$) and subsequently extended to the whole Galactic plane.

The first available Hi-GAL observations of the outer Galaxy, presented in Paper I, consist of four $2.^\circ3 \times 2.^\circ3$ adjacent tiles in the Galactic third quadrant. We will denote these with $\ell217$, $\ell220$, $\ell222$, and $\ell224$, respectively, according to the *Herschel* Data Archive nomenclature. These far-infrared maps of the outer Galaxy represent an ideal case for studying the structure of the ISM for two main reasons: the lower occurrence, in general, of compact bright sources and of star forming regions, and the lower degree of confusion along the line of sight.

The reduction procedure and the main characteristics of these observations are described in Paper I. Therefore, here we resume with only those features that are useful for the discussion in this paper. The observed wavebands are centered around 70 and 160 μm (PACS; Poglitsch et al. 2010) and 250, 350, and 500 μm (SPIRE; Griffin et al. 2010), with nominal resolutions of about $5''$, $12''$, $18''$, $25''$, and $36''$, respectively. The pixel sizes of these maps are $3.''2$, $4.''5$, $6.''0$, $8.''0$, and $11.''5$, at 70, 160,

[16] *Herschel* is a European Space Agency (ESA) space observatory with science instruments provided by the European-led Principal Investigator consortia and with important participation from NASA.

Table 1
Sizes in Pixels of the Investigated Images

Tile	70 μm	160 μm	250 μm	350 μm	500 μm[a]
ℓ217	1971	1403	1051	789	549
ℓ220	1951	1387	1041	781	545
ℓ222	1961	1395	1047	785	547
ℓ224	1977	1405	1055	791	551

Note. [a] The size of the column density maps is the same as that of the corresponding 500 μm maps.

250, 350, and 500 μm, respectively. The fields were observed by simultaneously acquiring PACS and SPIRE images in the five aforementioned photometric bands. This observing mode generally implies that the areas imaged by the two instruments are not exactly the same; in this paper, in particular, we consider only the common area of each tile, because we are interested in comparing the statistics of the same regions of the sky seen at different wavelengths.

The final images extracted at each wavelength for each tile are shown in Figure 1, where the color coding used to identify the different *Herschel* bands throughout the article is introduced. Since for a given tile the same area of the sky is considered in each band, the total number of pixels depends on the band; the size of each image in pixels is reported in Table 1.

The column density maps of each tile are analyzed here as well. They have been derived from a pixel-to-pixel modified black body fit, as explained in more detail in Paper I. To this end, first the maps were absolutely calibrated, correcting their zero level by means of offset values derived from the comparison with the Planck/IRAS data Bernard et al. (2010). Then, the 160, 250, and 350 μm maps were reprojected onto the grid of the 500 μm ones. The 70 μm maps were not involved in this calculation because they can contain emission coming from the so-called very small grains (Compiègne et al. 2010), not at thermal equilibrium, and/or from warmer spectral components, such as the proto-stellar content of the clumps, reflection nebulae, etc. For these reasons, the column density maps we obtained are more suitable to describe the cold component of dust in these regions. At a first glance, they look very similar to the SPIRE maps, and in particular to the 500 μm ones, having also the same resolution: both of these aspects turn out to be important for the spatial analysis reported in the following sections.

The four tiles show the presence of star forming activity, but ℓ217 and ℓ224 contain the brightest and most extended regions, mainly arranged in large filamentary shapes.

The knowledge of the kinematic distances of the clouds is somehow fundamental for identifying really coherent nebular structures, instead of superpositions of different distance components, to which the statistical descriptors can be applied. The distances for the Hi-GAL tiles analyzed here are obtained from CO(1–0) line observations carried out at the NANTEN submillimeter telescope (Mizuno & Fukui 2004), and presented in detail in Paper I. In detail, gas emission in the ℓ217 field is dominated by a component located at a kinematic distance of $\sim$2.2 kpc (see Table 1 of Paper I, their component II). CO emission is fainter in the ℓ220 tile, yet the component corresponding to the 2.2 kpc distance is still predominant.

Looking at the second row in Figure 1, the ℓ222 and ℓ224 tiles are found to be dominated by a bright component, corresponding to an average distance of $\sim$1.1 kpc, i.e., the so-called component I of Paper I. Two further distance components, III and IV, can be considered negligible in the present analysis. The former, located at an average distance of 3.3 kpc (therefore, likely in the Perseus arm) coincides with a bright region in the southeastern corner of the original ℓ222, which lies outside the region considered in this paper as a consequence of the tile cropping described above. The latter is constituted only by a bright, but small, portion of the ℓ217 field.

3. POWER SPECTRUM AND FBM IMAGES

The statistical descriptors we use in this paper revolve around the central concept of *power spectrum* $\mathcal{P}(\mathbf{k})$ of the observable $A(\mathbf{x})$, defined as the square modulus of its Fourier transform $\tilde{A}(\mathbf{k})$. The variable $\mathbf{x}$ is defined in an E-dimensional space, with $E = 2$ in the case of image analysis. A convenient approach is to study the shell-averaged power spectrum $\mathcal{P}(k)$, where $k = \|\mathbf{k}\|^2$. Because a power law is a distinctive experimental signature seen in a large variety of complex systems, frequently a search for a power-law behavior in the spectrum is carried out. An emblematic case is that of the Kolmogorov's power spectrum of turbulence (Kolmogorov 1941), calculated for the velocity field of incompressible fluids; a dependence of $\mathcal{P}(k) \propto k^p$ is expected, with $p = -11/3$ in three dimensions, $p = -8/3$ in two, and $p = -5/3$ in one, respectively. Different models, such as the classic Burgers' turbulence (e.g., Bec & Khanin 2007), still show similar power spectrums, though with different slopes ($p = 2$, Biskamp 2003). The presence of such a power-law behavior (in the full range of values of the k-wave number, or over a limited part of it) can be interpreted as an indication of turbulence and can suggest the characteristic scales at which both energy injection and dissipation take place.

The power spectra (or portions of them) of the ISM maps often exhibit a power-law behavior. The link with turbulence is quite natural: it is commonly accepted that a turbulent velocity field within the ISM can also shape the density field (cf. Boldyrev 2002; Padoan et al. 2003; Rowles & Froebrich 2011). However, it requires some care to derive the slope of the power spectrum. Indeed, the Fourier transform of a non-infinite mapped signal inevitably introduces unwanted frequencies due to the spatial sampling and limited size of the image (since the Fourier transform implicitly assumes wrap-around periodicity) leading to aliasing (Stutzki et al. 1998; Bensch et al. 2001). In the past, this has lead to the use of statistical tools that are more robust than the direct determination of a power spectrum. The improved performance of the new generation of observing instruments has allowed the production of maps with large numbers of pixels (as in the case of the Hi-GAL tiles), which might mitigate the aforementioned issues. Nevertheless, in this paper, we prefer to keep exploiting one of these indirect methods, namely the Δ-variance technique, briefly discussed in Section 4. In this way, we can both make possible a direct comparison with the literature and exploit further information that this technique can provide about the structure of the maps (see Section 4).

3.1. Fractional Brownian Motion Images

There is a category of stochastic fractals that can be helpful to test the statistical algorithms for structure analysis, since their Fourier transform has specific analytic properties which make them easy to be generated: the *fractional Brownian motion* (Peitgen & Saupe 1988). In the two-dimensional case, these show a good similarity to molecular cloud maps (Stutzki et al. 1998; Bensch et al. 2001; Miville-Deschênes et al. 2003; see also Figure 2). A detailed description of the fBm image properties is provided in Stutzki et al. (1998); here, we summarize only the

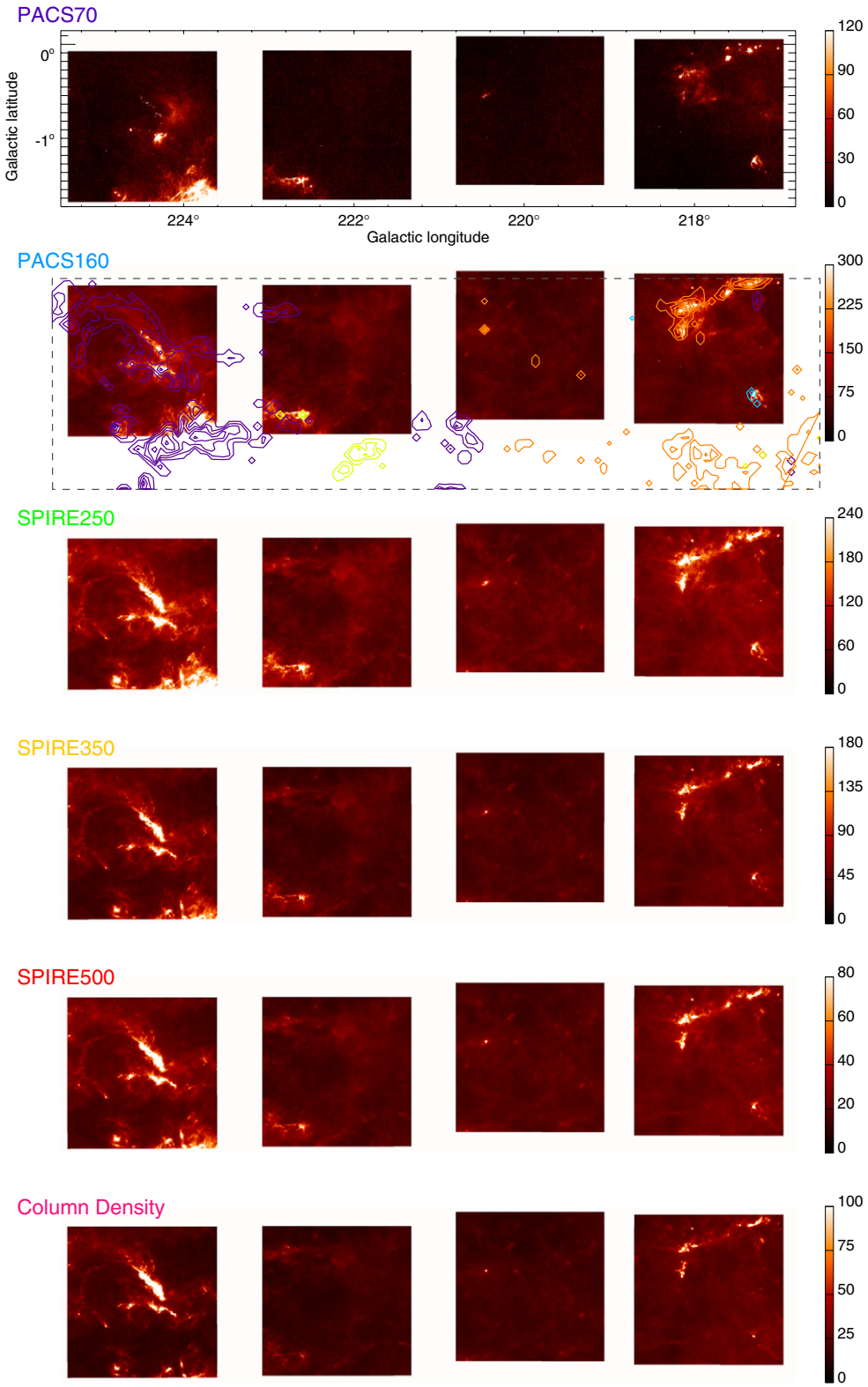

Figure 1. Fields investigated in this paper, divided by observed band. The instrument/wavelength combination is specified in each row (the column density maps are also shown in the last row), adopting a color convention which is used throughout the rest of the paper (blue: 70 μm, cyan: 160 μm, green: 250 μm, orange: 350 μm, red: 500 μm, magenta: column density). The color scales are linear, and the top value (corresponding to the white level) is chosen to allow a satisfactory visualization of the lower emission levels; the units are MJy sr^{-1} for the PACS and SPIRE maps, and 10^{20} cm^{-2} for the column density ones. The Galactic coordinate grid is displayed in the 70 μm case to show the displacement in the sky of the four considered tiles. The CO(1–0) contour levels (Paper I) are overplotted on the map at 160 μm. They start from 5 K km s^{-1} and are in steps of 15 K km s^{-1}. Components I, II, III, and IV are represented with purple, orange, yellow, and cyan contours, respectively. The area surveyed in CO(1–0) is delimited by a gray dashed line.

(A color version of this figure is available in the online journal.)

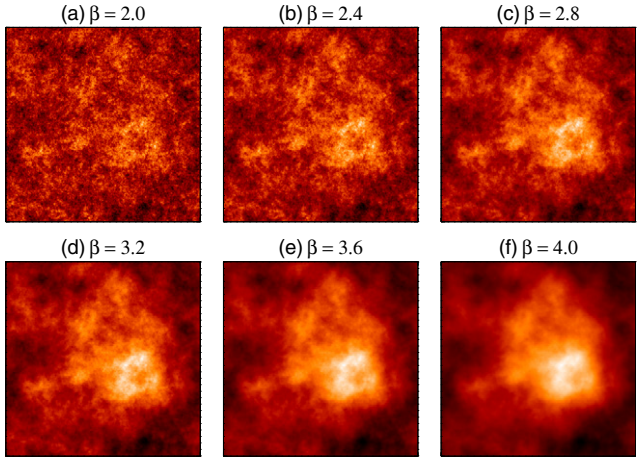

Figure 2. Synthetically generated fBm 300 × 300 pixels images, generated with increasing power spectrum slope, β, and starting from the same random phase distribution. Map units are arbitrary.

(A color version of this figure is available in the online journal.)

most relevant ones, which will prove to be useful in the analogy we make with ISM maps in the following sections. First, they are characterized by having a power-law power spectrum with exponent $\beta = E+2H$, where E is the Euclidean dimension of the considered space (for cloud maps, $E = 2$) and H is the so-called *Hurst exponent*, ranging from zero to one. Therefore, β can take values from two to four. Second, the phases of their Fourier transforms are random. Based on these two constraints, it is quite easy to obtain fBm images once β is assigned and a random phase distribution is generated.[17] In Figure 2, six 300 × 300 pixel fBm images are shown. They have the same phase distribution and differ only by β, which ranges from 2.0 to 4.0 in steps of 0.4. It can be seen that the phase distribution determines the overall appearance of the "cloud," but as β increases the structure becomes smoother and smoother due to the transfer of power from high to low spatial frequencies. We recall that the case $\beta = 0$ would correspond to *white noise*.

In terms of the fractal description, it has been shown that the fractal dimension of an E-dimensional fBm image is given by:

$$D = E + 1 - H, \tag{1}$$

so that the direct relation between D and β is:

$$D = \frac{3E + 2 - \beta}{2}. \tag{2}$$

An important property of the fBm images is that the power spectrum of the $(E - 1)$-dimensional projection on an E-dimensional fBm set is again a power law with the same spectral index (Stutzki et al. 1998). This result turns out to be important for establishing a link between the observed two-dimensional column density and the real three-dimensional cloud density field for clouds that can be considered isotropic, as suggested through theoretical arguments (Brunt et al. 2010) and empirical evidences (Federrath et al. 2009; Gazol & Kim 2010).

Thus, invoking Equation (2), it is found that

$$D_{E-1} = D_E - \frac{3}{2}, \tag{3}$$

i.e., the fractal dimension of an fBm object changes under projection by 1.5, not by 1 as one could erroneously expect.

[17] The fBm images generated in such a way are periodic, i.e., it is possible to place the image and its exact copy side by side and to connect with continuity the image to itself. Clearly, this cannot be the case of real ISM maps.

4. Δ-VARIANCE ANALYSIS

The Δ-variance method is a generalization of the *Allan variance* (Allan 1966), elaborated and characterized in detail by Stutzki et al. (1998). For a two-dimensional observable field $A(x, y)$, the Δ-variance at the scale L is defined as the variance of the convolution of A with a filter function, $\bigodot_L$:

$$\sigma_\Delta^2(L) = \frac{1}{2\pi}\left\langle \left(A * \bigodot_L \right)^2 \right\rangle_{x,y}, \tag{4}$$

where

$$\bigodot_L(r) = \begin{cases} \dfrac{1}{\pi(L/2)^2} & \left(r \leqslant \dfrac{L}{2}\right) \\ -\dfrac{1}{8\pi(L/2)^2} & \left(\dfrac{L}{2} < r \leqslant \dfrac{3L}{2}\right) \\ 0 & \left(r > \dfrac{3L}{2}\right) \end{cases} \tag{5}$$

is the *down-up-down cylinder* (or *French hat*) function and $r = \sqrt{x^2 + y^2}$. The two non-zero terms of the above definition represent the *core* and the *annulus* component of the filter, respectively.

Ossenkopf et al. (2008) recommended as a possible alternative to the French hat function to obtain a more reliable estimate of the spectral index, β, is to use the smoother *Mexican hat*, defined as

$$\bigodot_L(r) = \frac{4}{\pi L^2} e^{\frac{r^2}{(L/2)^2}} - \frac{4}{\pi L^2(v^2 - 1)}\left[e^{\frac{r^2}{(vL/2)^2}} - e^{\frac{r^2}{(L/2)^2}}\right], \tag{6}$$

where the two main terms in the right side of the equation represent the *core* and the *annulus* components, respectively, and v is the diameter ratio between them. To speed up calculations, the same authors suggest to perform the operation in Equation (4) as a multiplication in the Fourier domain,

$$\sigma_\Delta^2(L) = \frac{1}{2\pi}\int\int \mathcal{P}\left|\tilde{\bigodot}_L\right|^2 dk_x dk_y, \tag{7}$$

where $\mathcal{P}$ is the power spectrum of A, and $\tilde{\bigodot}_L$ is the Fourier transform of the filter function.

The fundamental relation that relates the slopes of Δ-variance and of the power spectrum (β) was shown by Stutzki et al. (1998):

$$\sigma_\Delta^2(L) \propto L^{\beta-2}. \tag{8}$$

Given the expression above, one can derive the power spectrum slope by performing a linear fit over the range of spatial scales for which the logarithm of Δ-variance manifests a linear behavior. In this work, we adopted this procedure following the prescriptions of Ossenkopf et al. (2008),[18] i.e., using a Mexican Hat filter with $v = 1.5$. Furthermore, we do not adopt any strategy based on assigning different weights to the pixels involved in the Δ-variance calculation, which is recommended by Ossenkopf et al. (2008) in case of maps characterized by a variable data reliability. The portions of the Hi-GAL maps we chose, indeed, being far from the tile boundaries, are characterized by quite uniform coverage (see also Traficante et al. 2011) and, consequently, by a stable rms noise.

[18] The IDL package for calculating the Δ-variance can be found at http://hera.ph1.uni-koeln.de/~ossk/Myself/deltavariance.html.

4.1. The Contribution of Compact Sources

From Equation (8) the Δ-variance behavior of an fBm image is expected to be a perfect power law. Although the ISM maps generally exhibit an fBm-like behavior (see Section 3.1), it is important to identify and characterize all of the signatures in the power spectrum ascribable to possible departures from the ideal fBm case, first of all, the presence of bright compact sources. For this purpose, we performed a test by simulating a PACS 160 μm map of a portion of the Galactic plane, using some typical parameters of this band, such as the pixel size of 4.″5. The steps of the recipe can also be followed in Figure 3, together with the effects they achieve on the corresponding Δ-variance curve.

1. A 2700 × 2700 pixel fBm background has been generated with a "typical" power spectrum slope $\beta = 2.5$ (see, e.g., Schneider et al. 2011). Therefore, to avoid dealing with a periodic image (see Section 3.1), this has been truncated, extracting a sub-image of 1800 × 1800 pixels.
2. To simulate the presence of very bright small regions, another 2700 × 2700 pixel fBm set has been generated with a significantly higher power spectrum slope ($\beta = 3.4$) and a different phase distribution. The resulting image has been exponentiated in order to enhance the high-signal regions. Again, a sub-image of 1800 × 1800 pixels has been extracted, making sure that the extracted image still contains the maximum of the original image. Finally, this has been added to the image obtained in (1), resulting in regions of enhanced brightness.
3. To reproduce the luminosity decrease off the Galactic plane, a modulation through a Gaussian profile has been applied. To make this profile more realistic, both the FWHM of the Gaussian and position of the peak slowly float as a function of the longitude, following a Gaussian distribution and a long-period sinusoid, respectively. A relevant decrease in emission moving away from the plane is more pronounced in the Hi-GAL observations of the inner Galaxy with respect to those considered in this work. However, the goal of this test is to qualitatively identify the effect on the Δ-variance curve of peculiar structures, thus it is instrumental to exacerbate these contributions.
4. A population of 500 compact sources has been spread across the map, generating random two-dimensional Gaussians whose size and peak flux distributions follow those found for the Hi-GAL field $\ell = 30^\circ$ (Elia et al. 2010). The probability of displacing a source in a given position of the map has been weighted with the intensity of the image in that position, to obtain a more realistic concentration of compact sources in regions with bright diffuse emission. Before co-adding the sources, the background image has been scaled by a given amount, such that its dynamical range gets similar to that of the $\ell = 30^\circ$ background at 160 μm. Finally, the image has been convolved with the PACS 160 μm beam and a low-level white noise is summed over, using an additional fBm image with $\beta = 0$.

In the right panels of Figure 3, the Δ-variance of the simulated images displayed on the left is plotted. All the images have been normalized between zero and one, to prevent overflows in calculation. As a consequences, the units of Δ-variance are arbitrary. We note that the Δ-variance slope is not affected by this rescaling. In step (1), the extracted sub-image curve (black line) shows a slightly steeper slope than that of the original set, plotted for reference (green line). While the latter line looks as expected, the former exhibits a linear behavior only over a limited range of scales (the gray area). The flattening of the curve at $L \gtrsim 2000''$ is due to the truncation of the original fBm set. Moving to step (2), a slope similar to the original one is still found on the limited range of scales $400'' \lesssim L \lesssim 1300''$ (darker gray area $\beta = 2.45$), while the steeper slope at $L \lesssim 400''$ is caused by the co-addition of the bright spots in the image. A further steepening is produced in step (3) by modulating emission with a low spatial frequency profile. This is particularly evident at the largest scales, where it compensates the flattening of the Δ-variance seen in the previous steps. Finally, the insertion of compact sources in step (4) is responsible for the appearance of a bump for $10'' \ll L \ll 100''$, which is the typical size range of the injected sources. This clearly corresponds, in light of the correspondence between Δ-variance and power spectrum, to the $\mathcal{P}_{\rm cirrus}(k)$ component of the power spectrum discussed by Miville-Deschênes et al. (2007) and Martin et al. (2010). Here, the diffuse emission behavior can be recovered only for a limited range of scales, since at the largest scales the effect is obviously still present due to the Galactic plane shape. At the smallest scales, on the other hand, a flattening of the Δ-variance curve is seen due to white noise (cf. Bensch et al. 2001). In any case, no physical information can be extracted at scales smaller than the instrumental beam.

Notice, however, that the significance of the effects described in this section depends on the analyzed map. For example, for the third Galactic quadrant maps we don't expect a strong influence on the Galactic plane shape. Furthermore, the bump in Δ-variance due to compact sources is likely not as sharp as that seen in Figure 3, because in the real maps the transition between a compact source and the surrounding cirrus emission is smoother than in our simulations. Larger clumps, H II regions, and filaments present in the real maps are additional intermediate structures between the two scale regimes of compact sources and the diffuse emission, contributing to the enlargement of the bump toward larger spatial scales and to a smoother connection with the linear portion of the Δ-variance. The importance of the filaments in the scenario of star formation and their ubiquity in the ISM have been highlighted by *Herschel* observations (e.g., Molinari et al. 2010a; Arzoumanian et al. 2011; Russeil et al. 2013; Schisano et al. 2013) and they are certainly mainly responsible for the departure of the images from fbm-like behavior at intermediate scales between compact sources and cirrus.

5. Δ-VARIANCE OF THE THIRD GALACTIC QUADRANT Hi-GAL FIELDS

After normalizing, as described in Section 4.1, the Hi-GAL maps shown in Figure 1, the Δ-variance versus spatial lag curves have been computed. They are plotted in Figure 4 using the color-band coding introduced in Figure 1.

5.1. General Results

Some general considerations can be drawn from the global trends exhibited by these curves. The lack of a sufficient level of diffuse emission in the 70 μm maps influences the corresponding Δ-variance spectrum, which shows peculiar trends compared with other wavelengths. Therefore, the curves at this wavelength are plotted only for completeness and the corresponding slopes are not shown. Only as a general remark, we notice that in the tiles ℓ217 and ℓ224, namely those with a significant emission of compact emission at 70 μm, a bump is present, peaking at

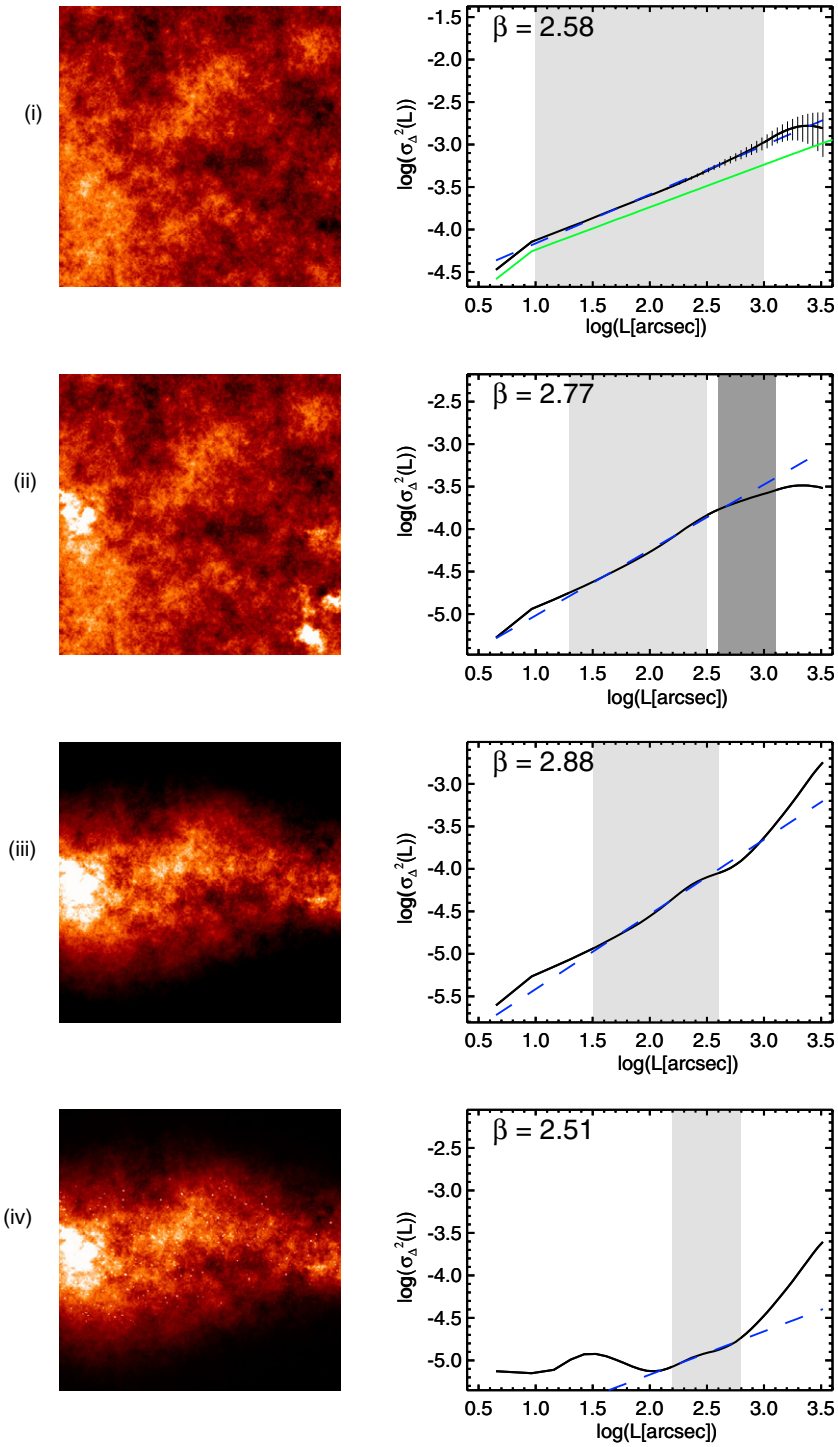

Figure 3. Simulation of a Hi-GAL image in four main steps (left panels) and corresponding Δ-variance plots (right panels). Step (1): an 1800 × 1800 pixel fBm image is generated as a background. Step (2): the brightness of a few limited regions is enhanced. Step (3): the characteristic shape of the Galactic plane is introduced through a Gaussian profile. Step (4): 500 Gaussian compact sources are spread across the map and a low-level white noise is finally added. The Δ-variance curves are plotted in the right panels. The *x*-axis variable is the decimal logarithm of the spatial lag, *L*, (expressed in arcseconds) and the range is the same for all panels. The range on the *y*-axis is different for each panel but its width has been kept the same in all panels to allow a visual comparison of the slopes. The Δ-variance is represented as a black solid line, while the linear fit over the inertial range (i.e., the range where the curve has a power-law behavior, here highlighted with a gray area) is plotted as a blue dashed line. In the top right panel, the Δ-variance of the larger original fBm set is also plotted as a green solid line. In the same panel, the error bars associated with the Δ-variance values are shown by way of example.

(A color version of this figure is available in the online journal.)

about 40″ and 25″, respectively. At larger spatial scales, in all cases, the 70 μm curves appear as slopes smaller than those of the larger wavelengths and are even negative in three cases out of four. This behavior is expected in the presence of low signal-to-noise ratio in the maps, keeping in mind Equation (8) and the white noise ($\beta = 0$) borderline case for the power spectrum slope.

For the remaining wavebands and for the column density maps, only one common linear range has been identified for each tile. Note that scales shorter than 100″ have not been considered

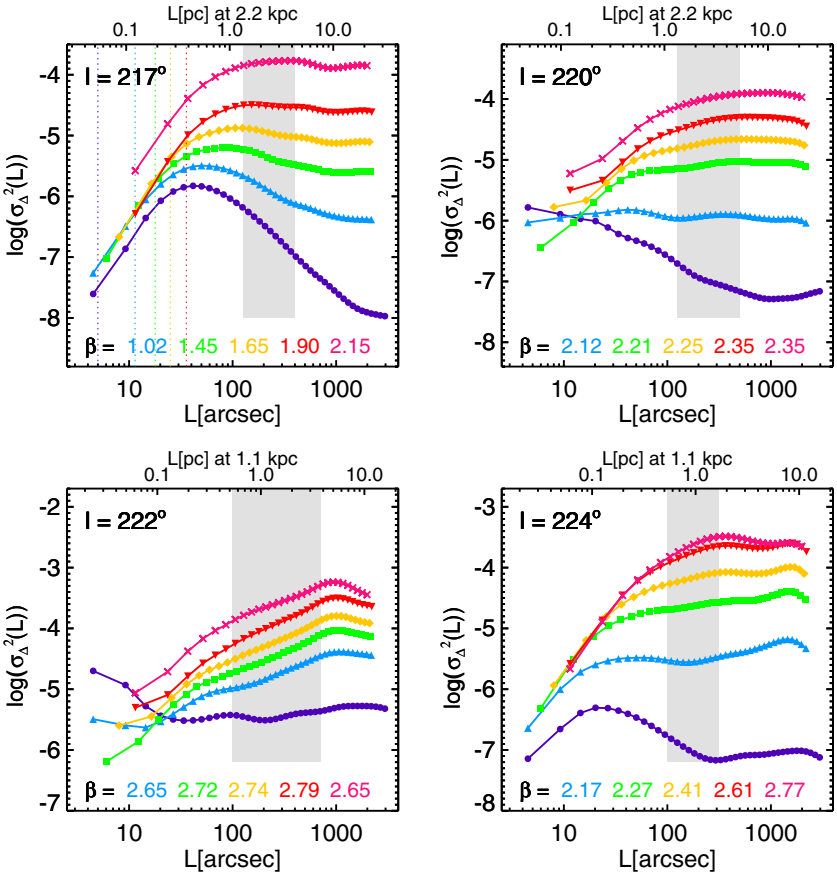

Figure 4. Δ-variance curves of the maps shown in Figure 1, using the same tile naming and band-color encoding. Also, in this case, we use the same *x*-axis range in all panels, and the same range width for the *y*-axis, to allow a direct comparison of the slopes. The inertial range is highlighted as a gray area. The corresponding linear slopes are transformed in power spectrum slopes through Equation (8) and reported on the bottom of each panel (except for 70 μm). Finally, for reference, the spatial scales corresponding to the nominal beams at each band are plotted as dotted lines in the top-left panel; scales below them are meaningless.

(A color version of this figure is available in the online journal.)

because of the possible contamination by compact sources. The curvature of each line, defined as $c = (\sigma_\Delta^2)''/\{1+[(\sigma_\Delta^2)']^2\}^{3/2}$ has been estimated by allowing only ranges where reasonably low values of $|c|$ are found.[19] This procedure keeps the extremes of the range far from possible peaks of the curve (e.g., in ℓ222), where the most relevant departure from linearity is expected.

The estimated fitting ranges and the corresponding slopes of the power spectrum (obtained from the Δ-variance slopes through Equation (8)) are reported in Figure 4 and summarized in Table 2, together with the corresponding fractal dimensions of the maps (derived through Equation (2)).

As a general remark on some evident trends found in all of the four tiles, we notice that, from the qualitative point of view, for each tile, the three SPIRE bands have similar spectral behaviors, whereas the general shape of the PACS 160 μm curves appear relatively different. More importantly, a systematic increase of the slope with the wavelength is found from 160 to 500 μm. This suggests not only that the emission morphology changes when observed at different wavelengths, but that its statistical properties are found to be different also. In particular, at 160 μm the contribution of warmer very small grains can still be relevant (Compiègne et al. 2010) and seems to be responsible for a more uniform distribution of the power of the image through the different spatial scales, resulting in a shallower β. In other words, the warmer dust turns out to be more diffuse and spread around than the cold dust, which is expected to be preferentially concentrated in denser environments like filaments (e.g., Padoan et al. 2006; Campeggio et al. 2007), producing a global smoothing of the observed emission features.

This effect can represent a possible explanation for the systematic discrepancy, found by Schneider et al. (2011), between the Δ-variance slope of A_V and ^{13}CO maps (shallower and steeper, respectively) of the same areas of the sky. These two tracers most likely do not describe the same components of the ISM in the same manner (e.g., Goodman et al. 2009). Moreover, the ISM is optically thinner at the SPIRE wavelengths than at 160 μm, so at long wavelengths one expects a more enhanced contrast between emission from high-density and low-density regions, resulting in a possible steepening of the power spectrum (and, equivalently, of the Δ-variance). However this reasoning could be too simplistic, because moving toward SPIRE wavelengths, a number of cold, small-scale filaments can manifest themselves, thus contributing to the power spectrum and counter-balancing the effect described above.

Another consideration concerns the Δ-variance of the column density maps: although the maps look quite similar to the SPIRE ones, the power spectrum behavior is generally found to be

[19] In reality, only few Δ-variance curves exhibiting no linear behavior in the common inertial range, e.g., the one of 160 μm of ℓ224, have not been considered in the evaluation of the linear range. However, despite these exceptions, the constraint we apply on the linear range appears more robust than the qualitative criteria adopted in the literature.

Table 2
Power Spectrum Exponent and Fractal Dimension of the Investigated Hi-GAL Maps

Field	Distance	Fit Range	β					D				
	(kpc)	(pc)	160 μm	250 μm	350 μm	500 μm	Col. Dens.	160 μm	250 μm	350 μm	500 μm	Col. Dens.
ℓ217	2.2	1.3–4.2	1.02	1.45	1.65	1.90	2.15	3.49	3.27	3.17	3.05	2.93
ℓ220	2.2	1.3–5.3	2.12	2.21	2.25	2.35	2.35	2.94	2.89	2.87	2.83	2.83
ℓ222	1.1	0.5–3.8	2.65	2.72	2.74	2.79	2.65	2.67	2.64	2.63	2.61	2.68
ℓ224	1.1	0.5–1.7	2.17	2.27	2.41	2.61	2.77	2.91	2.86	2.79	2.70	2.61

slightly different. Nonetheless, all the slopes we discovered lie in the typical range of values found for clouds studied in previous works (Bensch et al. 2001; Schneider et al. 2011; Rowles & Froebrich 2011; Russeil et al. 2013).

5.2. Results of Individual Maps

Going into detail of single tiles, we start from the westernmost field, ℓ217, associated with distance component I (see Figure 1). As in the case of ℓ224 discussed in the following, the abundance of compact sources and filaments in this field produces a visible bump at $L \lesssim 100''$ (see Section 4.1) at all wavelengths, whose peak and upper endpoint shift toward larger scales with increasing wavelength. This is generally followed by a descending trend which stops around 1000″, corresponding to a physical scale of ∼11 pc at a distance of 2.2 kpc. The presence of the large filament associable with Sh 2-287 (Sharpless 1959) in the northern part of the map is probably responsible for this slope change and for the departure of the maps from self-similarity at smaller scales.

The ℓ220 tile exhibits a more extended range of linearity. In fact, in the data set we consider, this tile has the poorest of bright features, therefore, the cirrus component can be thoroughly probed. The inertial range (1.3–5.3 pc) partially overlaps those found by Schneider et al. (2011) for some low-mass star-forming clouds. A good correspondence is also found with the *Herschel*-based analysis of the NGC 6334 star-forming region ($d = 1750$ pc) of Russeil et al. (2013), where three out of four separate sub-regions exhibit inertial ranges similar to that of ℓ220. At longer scales, around 15 pc, the Δ-variance curves flatten, which does not seem to correspond to any of the visible structures in the maps, such as filaments, ridges, or bubbles (and corresponding cavities). In this case it is likely that the upper limit of the self-similarity range is really correlated with the injection scale of turbulence.

In tile ℓ222 the steepest β slopes are found, over an inertial range of 0.5–2.7 pc. As in the case of ℓ220, the small number of bright features in the maps translates into a wide range of linearity of the Δ-variance and into a weak compact source bump. A peak is present at ∼1000″ (5.4 pc at $d = 1.1$ kpc), corresponding approximately to one-sixth of the map size. Although we do not have sufficient information to claim that this feature is associated with the bubble located on the east side of the tile (see Figure 1), we believe that this structure is responsible for the high values of β we find: indeed it generates a certain degree of segregation between relatively empty and bright regions (compare, for example, panels b and d of Figure 2), hence a transfer of power toward large scales.

Finally, for ℓ224, similarly to ℓ217, we find that the contribution of compact sources and filaments introduces features in the Δ-variance curves that make it difficult to identify a possible inertial range. The one we find between 0.5 and 1.7 pc (neglecting the 160 μm curve) is compatible with that of ℓ222. The slopes are generally steeper than those of the component II tiles, but shallower than those of ℓ222.

This comparison suggests that the region of the plane covered by the eastern tiles (ℓ222 and ℓ224), which is quite coherent from the kinematical point of view being associated with distance component I, show some common global statistical properties, different from those of the western tiles (ℓ217 and ℓ220, component II), generally characterized by shallower slopes. Furthermore, within the two distance components, the tiles containing bright features (ℓ217 and ℓ224, respectively) show slopes shallower than those of the corresponding low-emission tiles (ℓ220 and ℓ222, respectively).

Anyway, the variety of power-spectrum slopes we find in different tiles reinforces the scenario of the non-universality of the ISM fractal properties. From the morphological point of view, this corresponds to a different distribution of the power of the image on a spatial frequency range. From the point of view of the underlying physics, different power spectrum slopes are related to different conditions of the compressible turbulence, which is widely considered the most realistic situation in the ISM, especially in the presence of star formation (Henriksen & Turner 1984; Padoan & Nordlund 2002). Unlike the "rigid" results of the Kolmogorov (1941) incompressible turbulence (see Section 3), the compressible one is able to produce, in the ISM, a variety of morphologies and hence of power spectrum profiles (Federrath et al. 2009).

5.3. The Fractal Dimension of the Images

The fractal dimension, D, is another important observable, useful to characterize the ISM morphology. As mentioned in Section 1, several computational approaches have been adopted to derive it. Here, we use Equation (2), assuming that the analyzed maps have an fBm-like behavior in the recognized inertial ranges. This makes the descriptions based on β and D completely equivalent, however, speaking in terms of the fractal dimension allows us to make further comparisons with observational and theoretical results present in the literature. An overview of possible alternative methods for calculating the fractal dimension is provided in the Appendix.

The linear relation between the power spectrum slope, β, and the fractal dimension, D, contained in Equation (2) clearly expresses the intuitive concept that a "smoother" texture (high β, see Figure 2) must correspond to a lower degree of fractality (i.e., low D). The factor, $\frac{1}{2}$, appearing in the equation can split the perception of the variation of D in half, which is in fact expected to vary only between two and three. Although in the literature a variation of 0.1–0.2 between two values of D is presented as negligible, it actually corresponds to significant structural differences of the maps. In this respect, the fractal dimensions reported in Table 2 reassert (1) the decrease of D at increasing observed wavelength (already discussed as an increase of *beta*

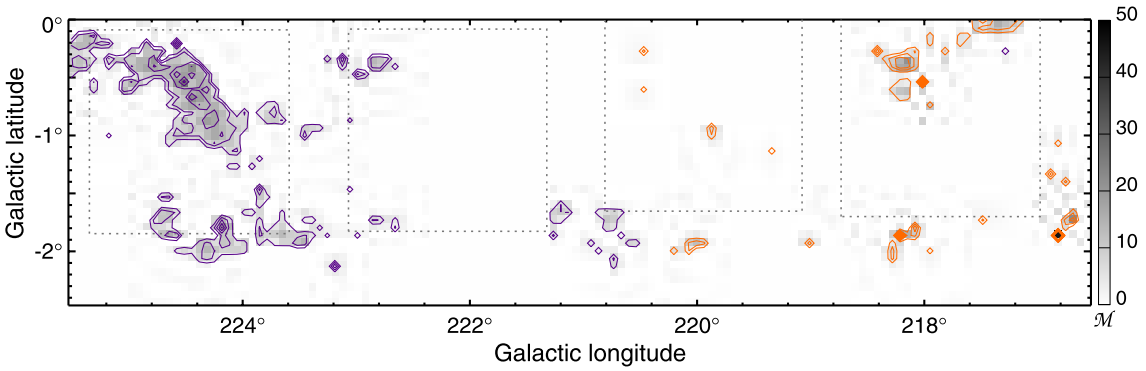

Figure 5. Grayscale map of the Mach number for distance components I and II (identified with purple and orange contours, respectively) of Paper I, calculated across the entire NANTEN available data cube as described in the text. Contours range from 5 to 30 in steps of 5. The gray dotted squares enclose the four areas investigated in this paper.

(A color version of this figure is available in the online journal.)

in Section 5.1) and (2) the significant differences between the structure observed in the western and eastern tiles.

In the three tiles showing fractal behavior (ℓ220, ℓ222, and ℓ224), all the values we derived range from $D = 2.61$ (500 μm of ℓ222 column density of ℓ224) to $D = 2.94$ (160 μm of ℓ220), and most of them are compatible with the typical range of variability found through statistical techniques (Rowles & Froebrich 2011; Schneider et al. 2011, and references therein), but also mostly with the $2.6 \lesssim D \lesssim 2.8$ found by Sánchez et al. (2007, 2009) through the perimeter–area relation.

Instead, the values we obtained are significantly larger than the average value found on IRAS 100 μm maps by Miville-Deschênes et al. (2007; $\beta = 2.9$, which is $D = 2.55$ in the fBm approximation), in particular those found at 160 μm, which is the closest band to the IRAS 100 μm one.

In any case, the values we find are far away from the first estimates of the fractal dimension of interstellar clouds ($D = 2.3$; Falgarone et al. 1991; Elmegreen & Falgarone 1996; Elmegreen 1997a), which initially described a quite constant and universal behavior of the ISM structure, and were found also to be in good agreement with the predictions of the Kolmogorov incompressible turbulence ($\beta = 3.6$ for the density field, then $D = 2.2$; Falgarone et al. 1994). Instead, the values found here, as well as the others obtained through the Δ-variance (Schneider et al. 2011, and references therein), are more compatible with the power spectra slopes of compressible turbulence, (e.g., Federrath et al. 2009), and in particular for the case of solenoidal driving of turbulence ($\beta = 2.89$, $D = 2.55$).

We can also compare with the theoretical predictions of Gazol & Kim (2010) on the power spectrum of both three-dimensional and column density in turbulent thermally bistable flows.[20] Their slope (calculated between 7 and 25 pc, i.e., a range of scales larger than ours) gets shallower as the Mach number increases: from $\beta = 2.64$ at $\mathcal{M} = 0.2$ to $\beta = 2.11$ at $\mathcal{M} = 4.0$ (a similar trend can also be clearly found in Kritsuk et al. 2006; Kowal et al. 2007). Although these simulations essentially reproduce the HI emission and despite the different investigated spatial ranges, the behavior we find suggests that the two eastern fields are characterized by smaller Mach numbers. In turn, the star formation efficiency of a cloud is recognized to inversely depend on the Mach number, whose contribution, however, can be found to be concomitant and then surpassed by that of other physical factors (e.g., Rosas-Guevara et al. 2010).

To investigate this aspect in our data, we derived the three-dimensional turbulent Mach numbers from the NANTEN data cube for the velocity components I and II, as the ratio between the local values of the deconvolved CO(1–0) line width $\langle\sigma_{\rm CO}\rangle$ and the sound speed c_s:

$$\mathcal{M} = \sqrt{3}\frac{\langle\sigma_{\rm CO}\rangle}{c_s}. \quad (9)$$

Here, $c_s = (kT/\mu)^{1/2} = 0.188(T/10\,{\rm K})^{1/2}$ km s^{-1}, where T is taken from the dust temperature maps obtained in Paper I simultaneously with the column density maps. The amount of CO spectra suitable for this analysis is limited by few constraints. First, only lines with a reasonable signal-to-noise ratio are considered (see details in Paper I); second, the line full width at half maximum must be larger than the spectral resolution element ($\Delta v = 1$ km s^{-1}) to allow deconvolution; third, the location of CO spectra must lie within one of the four fields we investigate in this paper. These are shown in Figure 5 (left panel), overlaid to the distribution of the Mach number across the entire NANTEN data set.

We note that we can derive meaningful statistical information only for the brightest regions, while the observations are not sensitive enough to trace the cirrus component, which is the one showing the self-similar behavior that justifies such a test. For this reason, we stress that observations with better sensitivity and spectral resolution are required for confirming this result.

We recall that in Paper I the distance components I and II have been found to differ in star formation efficiency by a factor of two (0.008 against 0.004, respectively). Interestingly, a direct correspondence between a larger fractal dimension and a higher star formation efficiency is found in this case. Unfortunately, the inconclusive argument of the Mach number cannot support the aforementioned theoretical picture, so that further checks are required and will be feasible when star formation efficiencies will be available for other portions of Hi-GAL.

From this discussion, it clearly emerges that the estimation of the fractal dimension of far-infrared dust emission from interstellar clouds (or portions of them) constitutes a further constraint to be put on theoretical models of cloud structure. In this sense, the vast amount of data provided by the multi-wavelength Hi-GAL survey represents a real minefield which can be searched for such observables.

[20] A gas in which temperatures above and below a given instability range can coexist in thermal pressure equilibrium is called bistable (see Gazol et al. 2005, and references therein). The atomic ISM is generally believed to be bistable.

5.4. Cloud Structure and Clump Mass Function

The quantitative indications obtained in the previous sections allow us to probe a relation derived by Stutzki et al. (1998), linking the power spectrum of the ISM to the mass function of the clumps (CMF hereinafter) which originate from such a structure. Indeed, as mentioned in Section 1, these authors showed that the fractal description of the ISM and the approach based on a hierarchical decomposition (e.g., Houlahan & Scalo 1992) are compatible. Stutzki et al. (1998) demonstrated that, for an fBm-like cloud characterized by a power-law power spectrum with slope β, assuming a clump mass spectrum in the cloud $dN/dM \propto M^{-\alpha}$ (in its high-mass end) and a relation between the clump mass and size as $M \propto r^{\gamma}$,

$$\beta = (3 - \alpha)\gamma. \quad (10)$$

This theoretical relation contains the intuitive concept that, once γ is fixed (where the cases $\gamma = 3$ and $\gamma = 2$ indicate clumps with constant volume and column density, respectively), a steeper power spectrum corresponds to a power transfer toward larger scales, hence to the presence of bigger clumps, which makes the CMF shallower.

Thus far, Equation (10) has been tested on very few data sets due to the lack of observational constraints, namely the simultaneous knowledge of the power spectrum and the CMF of a cloud. Stutzki et al. (1998) combined the "average" slopes β and α found for a sample of molecular clouds ($\beta = 2.8$ and $\alpha = 1.6$–1.8, respectively), deriving $\gamma = 2$–2.33. More recently, Shadmehri & Elmegreen (2011) explored this relation, analyzing three-dimensional fBm synthetic clouds, starting from the assumption that molecular clouds have on average $\beta = 2.8$ (different, however, from the shallower slopes we find in ℓ217 and ℓ220).

Here, it is possible to check this relation using the estimates of β for the investigated fields and exploiting the clump masses derived in Paper I to build a statistically significant CMF by selecting the sources as follows. First, it makes sense to consider only pre-stellar cores, namely starless sources gravitationally bound (i.e., those exceeding their corresponding Bonnor–Ebert mass, see, e.g., Giannini et al. 2012). Second, the considered source samples should be coherent from the spatial point of view, namely all the sources should belong to a physically connected region, following the steps described in Paper I for 398 compact sources associated with the closest velocity component (I), which is the component dominating the ℓ222 and ℓ224 fields. Here, we also consider component II for comparison, identifying 131 sources suitable for this analysis. The amounts of sources associated with components III and IV, on the other hand, are not statistically relevant to extend the analysis. The slope of the CMF for component I has already been estimated in the Paper I as $\alpha_{\rm I} = 2.2 \pm 0.1$, using an algorithm independent of the histogram binning (Olmi et al. 2013, and references therein) which also allows us to determine the lower limit of the validity range of the power law. Similarly, for component II, here we obtain $\alpha_{\rm II} = 1.9 \pm 0.1$ (Figure 6, panel a).

For the power spectrum slopes, we decided to use the values obtained for the column density maps of the two tiles characterized by low contamination of compact sources, namely ℓ220 for component I and ℓ222 for component II, respectively. Thus, we assume $\beta_{\rm I} = 2.65$ and $\beta_{\rm II} = 2.35$ for components I and II, with error bars of 0.1, and we get $\gamma_{\rm I} = 3.4 \pm 0.2$ and $\gamma_{\rm II} = 2.2 \pm 0.1$, respectively.

A comparison between these results and the observational mass versus radius relation can be performed using the same sources identified for building the CMFs of components I and II (Figure 6(b)). However, the distributions are affected by a significant dispersion and lack of a clear power-law trend, as noted in previous analyses of this kind (e.g., André et al. 2010; Giannini et al. 2012), so no clear-cut conclusion can be reached. Indeed, the lack of a definite scaling relation is indicative of a departure from pure self-similarity. Moreover, despite the fact that such clumps have been selected in order to build samples as homogeneous as possible, residual differences of physical and evolutionary conditions can be encountered. This might increase the scattering in the mass versus size plot, making it rather difficult to confirm the theoretically expected value for γ.

It is interesting, instead, to discuss the two very different values of γ that we find, especially in the context of the applicability of Equation (10) to various cases. The large discrepancy between these values depends on the different average β found for the two components, but mostly on the different values of α appearing at the denominator of Equation (10). The discrepancy between the CMF slopes of the two components can be justified, in turn, with

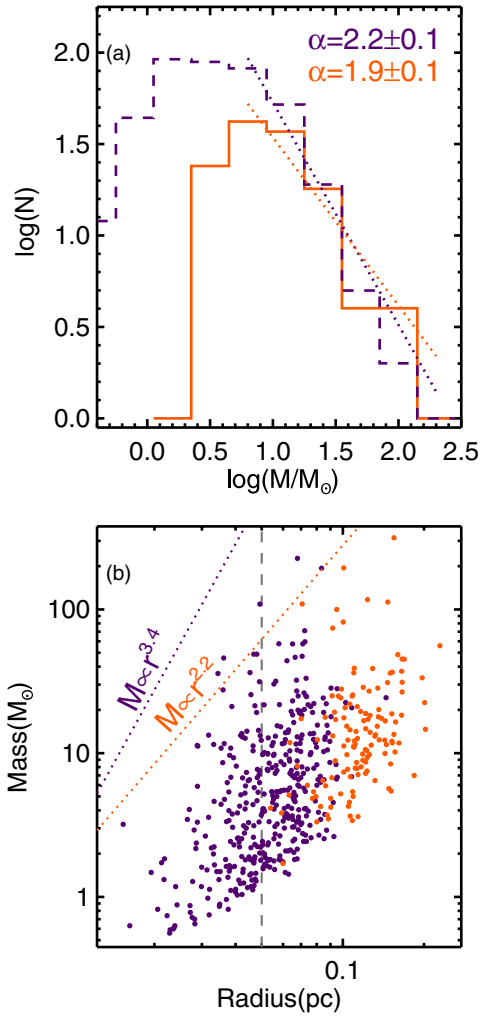

Figure 6. Panel (a): CMFs (solid histograms) of the pre-stellar clumps associated with the velocity components I (purple) and II (orange), respectively. Being the CMF in logarithmic form, the slope of the linear fit (dotted lines) corresponds to $\alpha - 1$, with α defined as in the text. Panel (b): mass vs. radius plot for the sources associated with components I and II (same colors as in panel a). The dotted lines represent the linear trends expected from Equation (10) (not to be confused with a fit to data). The gray dashed vertical line expresses the ideal transition between cores and clumps, according to the classification of Bergin & Tafalla (2007).

(A color version of this figure is available in the online journal.)

the relatively different intrinsic nature of the observed sources. Paper I discussed the fact that the detected compact sources, characterized by the same range of angular sizes (from one to few instrumental point spread functions), correspond to a variety of physical sizes depending on the source distance. In this case the typical factor, ∼2, between distances of component I and II sources is responsible of the clear segregation in size between the two populations, visible in Figure 6, panel b, such that the former are clumps, while the latter are a mixture of clumps and cores, according to the typical definition of these categories (e.g., Bergin & Tafalla 2007). It is widely acknowledged that the mass function slope of the cores is similar to that of the stellar initial mass function (e.g., André et al. 2010) and steeper than that of larger clumps (e.g., $\alpha = 1.6$–1.8; Kramer et al. 1998), as a consequence of the underlying fragmentation process. Samples characterized by contamination generally present intermediate slopes (e.g., Giannini et al. 2012). In this scenario, the CMF slope of the component II looks more similar to the case of the Polaris flare CO clumps ($\alpha = 1.8$; Heithausen et al. 1998) used by Stutzki et al. (1998) to derive a value of $\gamma = 2.3$. The component I source sample, on the contrary, consists of sources intrinsically smaller (as better resolved), closer to spatial scales where gravity dominates the morphology of the ISM, definitely stopping its scale-free behavior. As a consequence, in this case the applicability of Equation (10) turns out to be dubious.

These indications must be confirmed in the future by extending this kind of analysis to a larger variety of cases, offered by further Hi-GAL fields characterized by favorable observing conditions, typically found in the outer Galaxy.

6. SUMMARY

We have analyzed the first four fields of the outer Galaxy ($217^\circ \lesssim \ell \lesssim 225^\circ$, $-2^\circ \lesssim b \lesssim 0^\circ$) observed by *Herschel* as part of the Hi-GAL survey, to give a quantitative description of the structure of the far infrared diffuse emission. We exploited the power spectrum slope as a descriptor, and the Δ-variance algorithm as a tool to derive it in a robust way. The low degree of confusion along the line of sight, revealed by CO line observations, and both the resolution and the large size of the *Herschel* maps represent an ideal case to study the structure of the diffuse ISM on the Galactic plane. In this respect, the results of our analysis have a double value, because on the one hand we characterize the morphology of the ISM in this portion of the plane and on the other hand we provide a set of general prescriptions, considerations, and caveats for a possible extension of this kind of analysis to other *Herschel* maps. It is difficult in some cases to separate global from local results. Accordingly, in the following we try to summarize the conclusions going from the more general ones to those which have a more specific value:

1. The presence of compact sources in the maps affects the Δ-variance curves in terms of a bump up to scales of ∼100″. Other relevant effects are produced by the interruption of the self-similarity due to the Galactic plane latitude emission profile, and, on smaller spatial scales, to the presence of bright filaments and star forming regions. In our sample, however, these effects (especially the former) are less relevant than, for example, in the Hi-GAL fields of the inner Galaxy.
2. The maps obtained in four PACS/SPIRE wavebands (160–500 μm) for the investigated fields, together with the column density maps derived from them, show common features of the Δ-variance (or, equivalently, of the power spectrum), i.e., spatial scales corresponding to peaks and turn over points. However, the slope of the power spectrum can remarkably change from one band to another, generally increasing from 160 μm to 500 μm, probably due to a different spatial displacement of small against large grain dust components.
3. The obtained power spectrum slopes strongly vary from one tile to another, but remain in the typical range of slopes, $2 \lesssim \beta \lesssim 3$, calculated for different phases of the ISM by Schneider et al. (2011). The power spectrum, and the corresponding fractal dimension, are then far from being constant and universal as initially suggested by the analysis of the boundaries of the interstellar clouds (Falgarone et al. 1991). In two of the four investigated fields, the presence of regions of intense emission is responsible for a peak in the power spectrum, followed by a linear trend with a slope that is shallower than the case of the other two tiles, dominated by the cirrus.
4. None of these slopes are consistent with the Kolmogorov's incompressible turbulence case. We find that the model of supersonic isothermal turbulence with the solenoidal forcing of Federrath et al. (2009) seems more realistic, as already found by Schneider et al. (2011) using different tracers.
5. The power spectrum slopes of the two eastern fields, ℓ224 and ℓ222, are steeper than those of the western fields, ℓ220 and ℓ217. Each of these two pairs is dominated by the emission of a different distance component ($d = 1.1$ kpc and 2.2 kpc, respectively). Morphological differences of the density field suggest a higher degree of turbulence in the second component, also suggested by a lower star formation efficiency (yet not confirmed by the Mach number analysis). This represents an interesting evidence of the connection between fractality and star formation efficiency predicted by the theory.
6. We tested the linear relation, predicted for fBm-like clouds, between the mass function of the over dense structures (clumps) and the cloud power spectrum slope, using as a probe the exponent of the clump mass versus radius power-law relation. However, the mass versus radius distribution that we obtain is affected by significant dispersion and cannot be used to draw strong conclusions. Also, this relation seems to work better on the clumps at 2.2 kpc, while its predictions at 1.1 kpc are unrealistic, probably because the sample of clumps associated to this component is contaminated by cores.

Data processing and map production have been possible thanks to generous support from the Italian Space Agency via contracts I/038/080/0 and I/005/11/0. Data presented in this paper were also analyzed using the *Herschel* interactive processing environment (HIPE), a joint development by the *Herschel* Science Ground Segment Consortium, consisting of ESA, the NASA *Herschel* Science Center, and the HIFI, PACS, and SPIRE consortia.

During the preparation of this paper, D. E. lost his father, Elio Elia. D. E. is grateful for the example he set and his inborn and unconditional generosity. Nothing in D. E.'s career, including this paper itself, would have been possible without his father's steady support in many aspects of his life. This paper is dedicated to his memory.

Facility: Herschel (PACS, SPIRE)

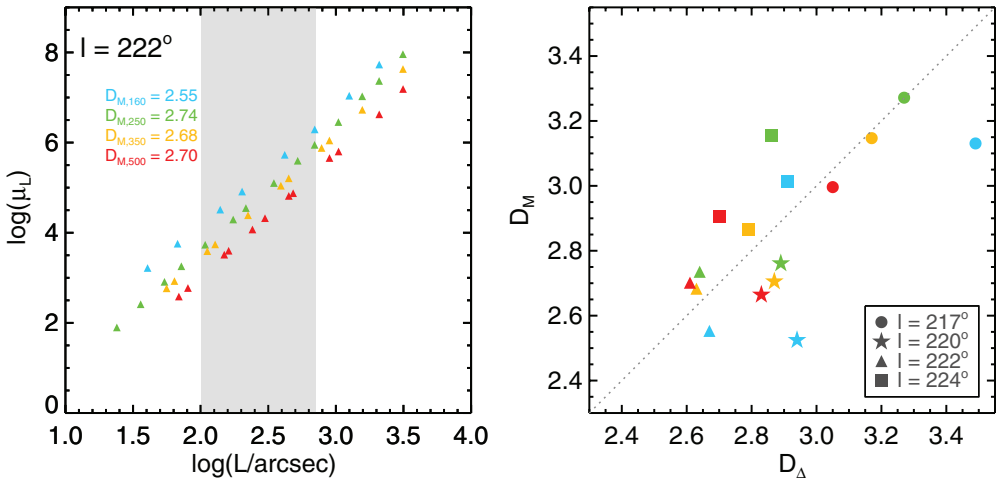

Figure 7. Left: average *volume* (see the text) occupied by the maps of ℓ222, plotted as a function of the investigated box size (reported to units of arcseconds to be comparable with the lag L used throughout the article). Tile naming and band-color encoding are the same as in Figure 1. Fractal dimensions correspond to the linear fit slopes of these series, estimated over the same scale range of Figure 4, bottom-left panel. They are reported in different colors, according to wavelength. Right: fractal dimensions of the maps analyzed in this paper (tiles from ℓ217 to ℓ224, wavelengths from 160 to 500 μm), derived through Δ-variance (x axis, from Table 2, here indicated with D_Δ to avoid confusion) and box counting techniques (y axis, see Appendix). The correspondence between tiles and symbol types is reported in the box at the bottom-right corner. The gray dotted line represents the bisector of the plane.

(A color version of this figure is available in the online journal.)

APPENDIX A

BOX COUNTING FRACTAL DIMENSION

In this paper, we followed the fBm approach to derive the fractal dimension, D, of the analyzed images from the analysis of their power spectrum, through Equation (2). Several other approaches might be used, however, to derive D for grayscale images. These can be seen as surfaces defined on a two-dimensional plane and embedded in a three-dimensional space ("mountain surfaces"). A fractal image, in particular, is a complex surface whose dimension is larger than two (as the Euclidean geometry would expect).

Methods aimed at estimating the fractal dimensions of the image intensity contour levels, such as the *perimeter–ruler* and the *area–perimeter* relation, are based on the distorted assumption that the image fractal dimension can be derived from the contour dimension simply by adding one. This immediately appears incorrectly in the case of highly anisotropic fractals, but also in more isotropic cases, such as the fBm sets (see Equation (3)) and simulated IS clouds (Sánchez et al. 2005).

Instead, considering the fractal set itself, it is possible to use approaches based on directly sampling the set with grids having different spacings. For example, the *box counting* approach is one of the most intuitive ways to derive the fractal dimension, and to understand its sense as well. Following Mandelbrot (1983), a three-dimensional cube containing the fractal surface $A(x,y)$ is partitioned into grids of cubes of variable size L. The number of volume elements occupied by the fractal set is a function of the element size: $N(L) \propto L^{-D_B}$, where D_B designates the box-counting fractal dimension, which can be obtained from the least square linear fit of the logarithms. However, whereas the estimate of $N(L)$ is rather trivial for binary fractal sets, it requires additional care in the case of gray-scale images such as ours. One possible approach consists of partitioning the (x, y) plane in a grid of squares (boxes) of size L, and estimating the difference between the maximum and the minimum values (normalized to integer multiples of L) achieved by the image in each box (Sarkar & Chaudhuri 1994). This is needed to estimate the *volume* spanned by the image in such a box. At each explored value of L, the average μ_L of the volume over all boxes is computed. Again, the so-called *mass fractal dimension* can be derived from the power-law scaling of μ_L:

$$\mu_L \propto L^{D_M} \tag{A1}$$

(Mandelbrot 1983).

For each tile and at each wavelength between 160 and 500 μm, we evaluated the linear fit in the same spatial scale range reported in Table 2. In Figure 7, left panel, an example of the D_M calculation is shown for the ℓ222 tile at four different wavelengths.

The comparison of the box-counting versus the Δ-variance-based fractal dimension of all the Hi-GAL maps analyzed in this article is shown in Figure 7, right panel. In most cases, a good agreement is found between the two methods at the SPIRE wavelengths, whereas strong discrepancies are found for PACS 160 μm, in at least three tiles out of four. It is possible that, being the 160 μm band, the one exhibiting the most evident departures from a linear (i.e., fractal) behavior (see Figure 4), estimating a univocal fractal dimension for maps at this wavelength is particularly difficult and plagued by strong uncertainties. In fact, it is well known that the Δ-variance is more sensitive to variations of the fractal behavior over different spatial scale ranges (Stutzki et al. 1998; Ossenkopf et al. 2008; Schneider et al. 2011), highlighted by distortions or local maxima/minima of the curves, so that a fractal dimension can be derived in a limited inertial range which is an integral part of the information. Instead, the curves obtained through box counting algorithms show linearity over larger scale ranges, as in Figure 7, left panel, but the corresponding fractal dimension represents a coarser description of the global statistical properties of the images.

REFERENCES

Allan, D. 1966, IEEEP, 54, 221
André, P., Men'shchikov, A., Bontemps, S., et al. 2010, A&A, 518, L102
Arzoumanian, D., André, P., Didelon, P., et al. 2011, A&A, 529, L6
Bec, J., & Khanin, K. 2007, PhR, 447, 1

Bensch, F., Stutzki, J., & Ossenkopf, V. 2001, A&A, 366, 636
Bergin, E. A., & Tafalla, M. 2007, ARA&A, 45, 339
Bernard, J.-P., Paradis, D., Marshall, D. J., et al. 2010, A&A, 518, L88
Biskamp, D. 2003, Magnetohydrodynamic Turbulence (Cambridge: Cambridge Univ. Press)
Boldyrev, S. 2002, ApJ, 569, 841
Brunt, C. M., Federrath, C., & Price, D. J. 2010, MNRAS, 405, L56
Campeggio, L., Elia, D., Maiolo, B. M. T., Strafella, F., & Cecchi-Pestellini, C. 2005, JPhCS, 6, 172
Campeggio, L., Strafella, F., Elia, D., et al. 2004, ApJ, 616, 319
Campeggio, L., Strafella, F., Maiolo, B., Elia, D., & Aiello, S. 2007, ApJ, 668, 316
Cartwright, A., Whitworth, A. P., & Nutter, D. 2006, MNRAS, 369, 1411
Chappell, D., & Scalo, J. 2001, ApJ, 551, 712
Compiègne, M., Flagey, N., Noriega-Crespo, A., et al. 2010, ApJL, 724, L44
Elia, D., Molinari, S., Fukui, Y., et al. 2013, ApJ, 772, 45
Elia, D., Schisano, E., Molinari, S., et al. 2010, A&A, 518, L97
Elmegreen, B. G. 1997a, ApJ, 480, 674
Elmegreen, B. G. 1997b, ApJ, 477, 196
Elmegreen, B. G. 2002, ApJ, 564, 773
Elmegreen, B. G., & Falgarone, E. 1996, ApJ, 471, 816
Elmegreen, B. G., & Scalo, J. 2004, ARA&A, 42, 211
Falgarone, E., Lis, D. C., Phillips, T. G., et al. 1994, ApJ, 436, 728
Falgarone, E., & Phillips, T. G. 1996, ApJ, 472, 191
Falgarone, E., Phillips, T. G., & Walker, C. K. 1991, ApJ, 378, 186
Federrath, C., Klessen, R. S., & Schmidt, W. 2009, ApJ, 692, 364
Federrath, C., Roman-Duval, J., Klessen, R. S., Schmidt, W., & Mac Low, M.-M. 2010, A&A, 512, A81
Gazol, A., & Kim, J. 2010, ApJ, 723, 482
Gazol, A., Vázquez-Semadeni, E., & Kim, J. 2005, ApJ, 630, 911
Giannini, T., Elia, D., Lorenzetti, D., et al. 2012, A&A, 539, A156
Goodman, A. A., Pineda, J. E., & Schnee, S. L. 2009, ApJ, 692, 91
Griffin, M. J., Abergel, A., Abreu, A., et al. 2010, A&A, 518, L3
Gustafsson, M., Lemaire, J. L., & Field, D. 2006, A&A, 456, 171
Heithausen, A., Bensch, F., Stutzki, J., Falgarone, E., & Panis, J. F. 1998, A&A, 331, L65
Henriksen, R. N., & Turner, B. E. 1984, ApJ, 287, 200
Houlahan, P., & Scalo, J. 1992, ApJ, 393, 172
Ingalls, J. G., Miville-Deschênes, M.-A., Reach, W. T., et al. 2004, ApJS, 154, 281
Khalil, A., Joncas, G., Nekka, F., Kestener, P., & Arneodo, A. 2006, ApJS, 165, 512
Kolmogorov, A. 1941, DoSSR, 30, 301
Kowal, G., Lazarian, A., & Beresnyak, A. 2007, ApJ, 658, 423
Kramer, C., Stutzki, J., Rohrig, R., & Corneliussen, U. 1998, A&A, 329, 249
Kritsuk, A. G., & Norman, M. L. 2004, ApJL, 601, L55
Kritsuk, A. G., Norman, M. L., & Padoan, P. 2006, ApJL, 638, L25
Mandelbrot, B. B. 1983, The Fractal Geometry of Nature/Revised and Enlarged Edition (New York: Freeman)
Martin, P. G., Miville-Deschênes, M.-A., Roy, A., et al. 2010, A&A, 518, L105
Miville-Deschênes, M.-A., Lagache, G., Boulanger, F., & Puget, J.-L. 2007, A&A, 469, 595
Miville-Deschênes, M.-A., Levrier, F., & Falgarone, E. 2003, ApJ, 593, 831
Mizuno, A., & Fukui, Y. 2004, in ASP Conf. Ser. 317, Milky Way Surveys: The Structure and Evolution of Our Galaxy, ed. D. Clemens, R. Shah, & T. Brainerd (San Francisco, CA: ASP), 59
Molinari, S., Swinyard, B., Bally, J., et al. 2010a, A&A, 518, L100
Molinari, S., Swinyard, B., Bally, J., et al. 2010b, PASP, 122, 314
Olmi, L., Anglés-Alcázar, D., Elia, D., et al. 2013, A&A, 551, A111
Ossenkopf, V., Esquivel, A., Lazarian, A., & Stutzki, J. 2006, A&A, 452, 223
Ossenkopf, V., Klessen, R. S., & Heitsch, F. 2001, A&A, 379, 1005
Ossenkopf, V., Krips, M., & Stutzki, J. 2008, A&A, 485, 917
Padoan, P., Boldyrev, S., Langer, W., & Nordlund, Å. 2003, ApJ, 583, 308
Padoan, P., Cambrésy, L., Juvela, M., et al. 2006, ApJ, 649, 807
Padoan, P., Cambrésy, L., & Langer, W. 2002, ApJL, 580, L57
Padoan, P., & Nordlund, Å. 2002, ApJ, 576, 870
Peitgen, H.-O., & Saupe, D. (ed.) 1988, The Science of Fractal Images, xiii + (New York: Springer-Verlag), 312
Pilbratt, G. L., Riedinger, J. R., Passvogel, T., et al. 2010, A&A, 518, L1
Poglitsch, A., Waelkens, C., Geis, N., et al. 2010, A&A, 518, L2
Rosas-Guevara, Y., Vázquez-Semadeni, E., Gómez, G. C., & Jappsen, A.-K. 2010, MNRAS, 406, 1875
Rosner, R., & Bodo, G. 1996, ApJL, 470, L49
Rowles, J., & Froebrich, D. 2011, MNRAS, 416, 294
Russeil, D., Schneider, N., Anderson, L. D., et al. 2013, A&A, 554, A42
Sánchez, N., Alfaro, E. J., & Pérez, E. 2005, ApJ, 625, 849
Sánchez, N., Alfaro, E. J., & Pérez, E. 2007, ApJ, 656, 222
Sánchez, N., Alfaro, E. J., & Pérez, E. 2009, RMxAA Conf. Ser., 35, 76
Sarkar, N., & Chaudhuri, B. 1994, ITSMC, 24, 115
Scalo, J. 1990, in Physical Processes in Fragmentation and Star Formation, ed. R. Capuzzo-Dolcetta, C. Chiosi, & A. di Fazio (Astrophysics and Space Science Library, Vol. 162; Dordrecht: Kluwer), 151
Schisano, E., Rygl, K. L. J., Molinari, S., et al. 2013, ApJ, submitted
Schneider, N., Bontemps, S., Simon, R., et al. 2011, A&A, 529, A1
Schneider, N., Stutzki, J., Winnewisser, G., & Block, D. 1998, A&A, 335, 1049
Shadmehri, M., & Elmegreen, B. G. 2011, MNRAS, 410, 788
Sharpless, S. 1959, ApJS, 4, 257
Sreenivasan, K. R., Ramshankar, R., & Meneveau, C. 1989, RSPSA, 421, 79
Stutzki, J., Bensch, F., Heithausen, A., Ossenkopf, V., & Zielinsky, M. 1998, A&A, 336, 697
Traficante, A., Calzoletti, L., Veneziani, M., et al. 2011, MNRAS, 416, 2932
Vavrek, R., Balázs, L. G., & Epchtein, N. 2001, in ASP Conf. Ser. 243, From Darkness to Light: Origin and Evolution of Young Stellar Clusters, ed. T. Montmerle & P. André (San Francisco, CA: ASP), 149
Vázquez-Semadeni, E. 1999, in Millimeter-Wave Astronomy: Molecular Chemistry & Physics in Space, ed. W. F. Wall, A. Carramiñana, & L. Carrasco (Astrophysics and Space Science Library, Vol. 241; Dordrecht: Kluwer), 161
Wilson, C. D., Howe, J. E., & Balogh, M. L. 1999, ApJ, 517, 174